Journal of Hazardous Materials 487 (2025) 137160

Contents lists available at ScienceDirect

Journal of Hazardous Materials

journal homepage: www.elsevier.com/locate/jhazmat

# Rapid electrothermal upcycling hexachlorobutadiene (HCBD) polluted distillation residue into turbostratic graphene for enhanced electromagnetic wave absorption

Tong Chen [a], Yunxiao Zhao [a], Hanyang Sun [a], Xinyu Niu [a], Pei Li [a,*], Yan Xia [a], Xiaoqing Lin [a], Xiaodong Li [a], Ying Wang [d], Jianhua Yan [a], Chen Sun [b,c,**]

[a] State Key Laboratory of Clean Energy Utilization, Institute for Thermal Power Engineering, Zhejiang University, Hangzhou 310058, China
[b] Institute of Zhejiang University - Quzhou, No. 99 Zheda Road, Quzhou 324000, China
[c] Key Laboratory of Biomass Chemical Engineering of Ministry of Education, College of Chemical and Biological Engineering, Zhejiang University, Hangzhou 310027, China
[d] Magnetism Key Laboratory of Zhejiang Province, China Jiliang University, Hangzhou 310018, China

## HIGHLIGHTS

- Pulse Joule heating was firstly proposed for HCBD remediation.
- The HCBD removal reached over 99 % in 10 s.
- Turbostratic graphene products were synthesized from polluted residues.
- Waste derived graphene demonstrated excellent EMW adsorption performance.

## GRAPHICAL ABSTRACT

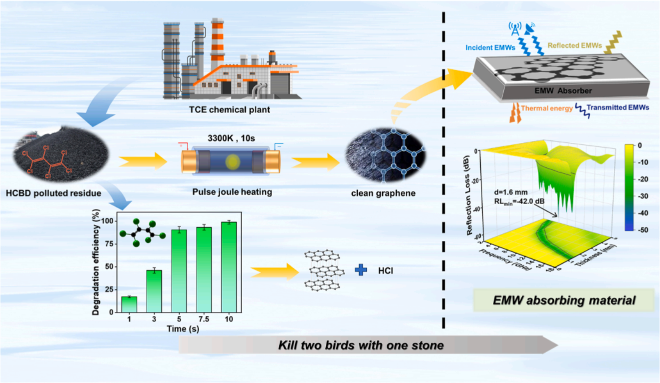

## ARTICLE INFO

*Keywords:*
Hexachlorobutadiene
Distillation residue
Pulse Joule heating
Turbostratic graphene
Electromagnetic wave absorption

## ABSTRACT

The trichloroethylene production industry generates high-boiling-point solid residues during rectification, which contain high concentrations of chlorinated contaminants, particularly hexachlorobutadiene (HCBD). Traditionally, these distillation residues are managed through co-incineration or landfilling, leading to environmental and economic challenges. In this study, we present a rapid and environmentally friendly electrothermal approach for both detoxifying and upcycling distillation residue into graphene-based electromagnetic wave (EMW) absorbing materials. By employing a DC power pulse discharge with a 10 s duration, we achieved over 99 % HCBD degradation efficiency. Characterization results indicate that the thermal shock transforms the distillation residue into high-value turbostratic pulse graphene (tPG). This tPG, featuring a unique structure, demonstrates

---

* Corresponding author.

** Corresponding author at: Institute of Zhejiang University - Quzhou, No. 99 Zheda Road, Quzhou 324000, China.

*E-mail addresses:* princeleego@zju.edu.cn (P. Li), sunchen1@zju.edu.cn (C. Sun).

https://doi.org/10.1016/j.jhazmat.2025.137160
Received 26 September 2024; Received in revised form 4 December 2024; Accepted 7 January 2025

substantial potential as an EMW absorber, with an effective absorption bandwidth of 3.9 GHz and a reflection loss of −42.0 dB at a minimal matching thickness of 1.6 mm. The method offers a sustainable, cost-effective solution for hazardous waste management, combining rapid processing with high-value material production.

## 1. Introduction

Hexachlorobutadiene (HCBD) was classified as one of the persistent organic pollutants (POPs) by the Stockholm Convention in 2015 and banned from production due to its significant threat to human health and the environment [1]. In 2017, unintentional emissions were further regulated under Annex C of the Stockholm Convention [2]. By 2023, HCBD was added to the Chinese government's List of Emerging Contaminants under Priority Management and Control [3]. According to both the Stockholm and Basel conventions, waste containing HCBD at concentrations above the low POP content (LPC) value (100 mg/kg) must be treated in a manner that ensures the destruction or irreversible transformation of POPs [4].

Currently, the primary source of HCBD is its unintentional production during the manufacture of chlorinated hydrocarbons, particularly the manufacture of trichloroethylene (TCE), perchloroethylene (PCE), and carbon tetrachloride (CTC) [5]. HCBD is often concentrated up to 5000 mg/kg in byproducts from the chemical industry, specifically in bottom residues or liquids during the production of chlorinated solvents [6]. For example, global production of TCE has reached 739,000 tons, resulting in approximately 59,000 tons of distillation residues [7,8]. These solid residues are typically dark in color, have a strong, pungent odor, and contain numerous impurities and toxic substances. In China, these residues have been listed in the "National Catalogue of Hazardous Wastes" (HW11), mandating special treatment.

The composition of these distillation residues varies depending on the raw materials used, but they typically contain aromatic compounds, hydrocarbons, hydrocarbon derivatives, and tar-like components with a high carbon content (around 40 %). Currently, landfilling and incineration are the primary two ways for distillation residue disposal. However, during landfilling, high concentration of chlorinated organic pollutants can leach into groundwater, and incineration can emit dioxins, leading to secondary pollution [9]. In light of the Paris Agreement's emphasis on combating global warming and advancing global carbon neutrality, there is an urgent need to explore innovative, low-carbon, high-efficiency, and environmentally friendly approaches for the treatment of chemical distillation residues.

Flash Joule heating (FJH) is a technique that heats feedstocks to temperatures as high as 3000 K within seconds through capacitance discharge. This technology has been applied in the synthesis of graphene from solid wastes[10–12], the recovery of precious metals [13], and the remediation of contaminated soil [14]. The flash heating process causes the instantaneous conversion of carbon sources, resulting in the formation of turbostratic few-layer graphene (tFG), which has a higher interlayer distance (3.45 A) compared to AB-stacked graphene (3.35 A). [10]. This characteristic enhances its exfoliation efficiency and dispersibility in composite materials [10]. Flash graphene has demonstrated numerous applications, including lubricant additives and composite reinforcement [15,16]. Additionally, during FJH remediation, carbon atoms from organic pollutants are converted into graphitic carbon rather than $CO_2$, promoting a carbon-negative process. The rapid cooling rate of FJH also helps prevent the formation of secondary persistent halogenated organic pollutants [14].

Given the high contents of HCBD and carbon contents in distillation residues (DR), herein, we reported a pulsed joule heating (PJH) process for detoxifying and upcycling the HCBD polluted DR. The process operates without the need for a furnace or solvent, and takes less than 10 s. The degradation of HCBD and other chlorinated organic pollutants was assessed using Gas Chromatography-Mass Spectrometry (GC-MS). Various characterization results confirmed the synthesis of turbostratic graphene. Lastly, to achieve "cradle to grave" utilization, the DR derived graphene was applied in EMW absorption (Fig. 1). The turbostratic structure induced by electrothermal effect results in an extreme low reflection loss, even at a minimal thickness, indicating great potential for electromagnetic absorption application. This work not only offers a simple method for purifying HCBD polluted distillation residues, but also provides a novel approach of upcycling hazardous wastes for advanced applications, such as anti-electronic reconnaissance, radiation shielding, and stealth technologies.

## 2. Materials and methods

### 2.1. Materials and chemicals

The distillation residue used in this work was collected from the distillation tower from a TCE and PCE co-production factory (Zhejiang Juhua Co., Ltd.) in Quzhou, Zhejiang Province. The factory employs an acetylene transformation method, which involves a multistage distillation process to refine chlorinated hydrocarbon products. The proximate and ultimate analyses of the initial raw material distillation residue were performed in accordance with the standards GB/T 212–2008[17] and GB/31391–2015[18], with the results summarized in Table 1.

Chemical reagents, including HCBD standard samples, hexane, methanol, petroleum ether (30–60 °C), and other analytical reagents were purchased from Sinopharm Chemical Reagent (Beijing, China). All chemicals were of analytical grade and used without further purification. Florisil (60 −100 mesh), Silica gel (0.063 −0.100 mm) and anhydrous sodium sulfate (purity > 99.5 %) were obtained from Shanghai Aladdin Biochem Technology Co., Ltd. Prior to use, Florisil was activated at 140 °C for 7 h and deactivated with 5 % water, while silica gel and sodium sulfate were heated at 600 °C for 6 h. Commercial graphene was purchased from Shanghai MacLean Company. Water was purified with a Milli-Q Integral water purification system from Merck Millipore (Darmstadt, Germany).

### 2.2. Pulsed Joule heating of distillation residue

Fig. 2a depicts the schematic diagram of a typical PJH reactor. In a typical batch, a mixture of DR (84 wt%) and carbon black (16 wt%) with a total mass of 150 mg was loaded into a quartz tube. Two graphite electrodes were loosely fitted into the quartz tube for outgassing. The resistance of the sample was controlled under 5 Ω by adjusting the two electrodes through screw rotation. The quartz tube was secured on the reaction stage and connected to a programmable DC power supply (3 kW). The reaction was carried out in a mild vacuum chamber (0.01 MPa). A two-stage pulsed discharge procedure was employed, starting with a pretreatment pulse of 30 V for 1 s and subsequently a 30 V pulse period for a certain time (1 ~10 s). During the discharge process, the temperature inside the quartz tube was monitored in real-time using an infrared (IR) thermometer. After the reaction, the resulting solid samples were named as tPG-X s for further characterization, X represented the discharge time of the second period.

Yields were determined by the mass ratio of tPG products to raw materials (DR), calculated by

$$Y_{tPG}(\%) = \frac{M_{tPG}}{M_{DR}} \times 100 \tag{1}$$

where $M_{tPG}$ and $M_{DR}$ represent the mass of solid products and raw materials, respectively. The yields for different PJH reaction times are listed in **Table S1**, and all yields are above 30 %.

### 2.3. Analytical method

The concentrations of HCBD and other chlorinated organic pollutants in the distillation residue and treated products were detected by the gas chromatography-mass spectrometry (GC-MS 8890–5977B, Agilent, U.S.A.). In this study, a rapid sample pretreatment procedure for the HCBD analysis in DR samples was developed, referencing the United States Environmental Protection Agency (EPA) Method 1613 and prior research [6]. Approximately 1 g of solid sample was extracted with 250 mL hexane at 100 °C for 16 h using Soxhlet extractor. The extract was concentrated to about 2 mL by rotary evaporation and then subjected to cleanup using a multilayer silica-Florisil composite column (15 mm inner diameter). This column was packed with 4 g of Florisil, 6 g of activated silica gel, and 3 g of anhydrous sodium sulfate, layered from top to bottom. The column was precleaned with 50 mL petroleum ether and then eluted with 150 mL petroleum ether in three aliquots after sample loading. The eluate was concentrated to 1 mL by rotary evaporation under a gentle nitrogen gas stream. Finally, 2 μL of the final extract was injected into the GC-MS for quantification. The optimized chromatographic and mass spectrometric conditions, as well as the elution solvents are detailed in the Supplementary Information.

During the sample pretreatment process, a laboratory blank sample was included in each batch of sample analyses. The test results for the blank samples showed that the target measurement values were all less than 5 % of the actual sample concentrations. This result confirms that the laboratory pretreatment process introduced minimal interference with the HCBD analysis, ensuring the reliability of the experimental results. The method detection limit (MDL) for HCBD, calculated as 3 times the signal-to-noise ratio, was 0.02 ng $g^{-1}$ dry weight for DR samples.

Degradation Efficiency (DgE) is a commonly used metric to measure the degradation of POPs, and its value is often reported as a percentage. The degradation efficiency in this study was calculated using the following formula:

$$DgE_{HCBD}(\%) = \left(1 - \frac{C_R}{C_0}\right) \times Y_{tPG} \times 100 \tag{2}$$

here, $C_0$ is the initial concentration of HCBD, $\mu g \cdot g^{-1}$; $C_R$ is the remaining concentration of HCBD, $\mu g \cdot g^{-1}$.

The distribution of chlorine after PJH treatment was categorized as four types: gas phase organic chlorine ($OrCl_{gas\ phase}$), gas phase inorganic chlorine ($InorCl_{gas\ phase}$), solid phase organic chlorine ($OrCl_{solid\ phase}$), and solid phase inorganic chlorine ($InorCl_{solid\ phase}$). The total chlorine in raw DR and derived graphene (solid phase) was determined through high temperature combustion hydrolysis method under pure oxygen in a tube furnace. The inorganic chlorine in fixed state samples was tested through water leaching method. The organic chlorine in solid phase was calculated according to Eq. (3). The emitted inorganic chlorine (HCl) was captured by a mixed solution of 0.01 M $NaHCO_3$ and 0.01 M $Na_2CO_3$ under $N_2$ atmosphere on the reactor shown in Fig.S6. The gas phase organic chlorine was calculated according to Eq. (4). The concentration of chlorides in the solution was subsequently analyzed using ion chromatography (IC) Detailed information is shown in Text S1.

$$OrCl_{solid\ phase} = TotCl_{solid\ phase} - InorCl_{solid\ phase} \tag{3}$$

$$OrCl_{gas\ phase} = TotCl_{raw\ DR} - InorCl_{gas\ phase} - TotCl_{solid\ phase} \tag{4}$$

Moreover, the organic pollutants emitted in the gas phase were also adsorbed using an adsorption tube (Tenax TA) and analyzed using GC-MS (8890–5977B Agilent, U.S.A.) (shown in **Fig.S7**).

### 2.4. Characterizations

Raman spectra were acquired in the range of 1000–3000 $cm^{-1}$ using a Renishaw inVia Raman microscope at an excitation wavelength of 532 nm. Thermogravimetric analysis (TGA) was conducted on the Mettler Toledo TGA/DSC 3 + system at a heating rate of 10 °C $min^{-1}$ under 100 mL $min^{-1}$ air flow. X-ray diffraction (XRD) was performed using the Rigaku SmartLab system over a range of 5 –80° and the scanning speed of 5°/min, respectively. X-ray photoelectron spectroscopy (XPS) was carried out using the Thermo ESCALAB250XI system. The system uses monochromatic Al Kα radiation (hv=1486.6 eV) for analysis. All XPS spectra were calibrated using the C1s peak at 284.8 eV as the reference. Scanning electron microscopy (SEM) and energy dispersive spectroscopy (EDS) were recorded using the FEI Inspect F50 system. Transmission electron microscopy (TEM) images were obtained on a Thermo Fisher Scientific, Talos F200X transmission electron microscope. The diffraction patterns were calibrated using an Al standard. UV–Vis diffuse reflectance spectra were obtained on a SHIMADZU UV-2450 spectrophotometer equipped with a photomultiplier tube in the detection range of 200–800 nm. Varying amounts of finely milled tPG-10 s, ranging from 1 to 10 g/L, were added to the 1 wt% Pluronic F-

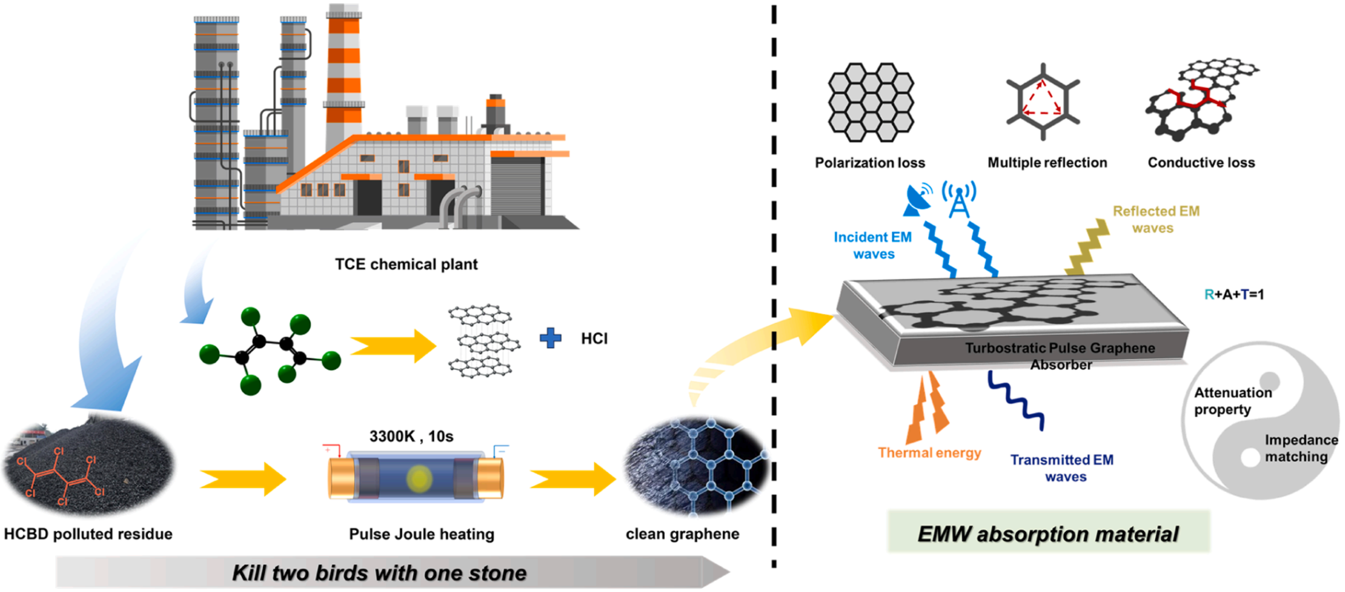

**Fig. 1.** Upcycling of HCBD polluted distillation residue to tPG for electromagnetic wave absorption.

127 aqueous solution. The mixture was sonicated in an ultrasonic bath at 25°C for 30 minutes to achieve a dark, homogeneous dispersion. The dispersion was then centrifuged for 20 minutes to remove any aggregates. The resulting supernatant dispersion was diluted 50 times, and the absorbance was measured at 660 nm. The concentration of graphene in the solution was calculated using an extinction coefficient of $\alpha_{660} = 6600\ L\cdot g^{-1}\cdot m^{-1}$. BET measurements were performed on a Quantachrome Autosorb IQ BET surface analyzer at 77 K, where $N_2$ was used as the adsorption/desorption gas.

### 2.5. *Electromagnetic wave absorption performance evaluation*

To investigate electromagnetic wave (EMW) absorption properties, the obtained specimens (10–35 wt%) were mixed with paraffin and compressed into a series of toroidal shapes (3.0 mm inner diameter and 7.0 mm outer diameter). Electromagnetic parameters were measured using an Agilent PNAN5244A vector network analyzer using the coaxial-line method from 2.0 to 18.0 GHz. The EMW absorption properties under metal backing conditions were calculated based on transmission line theory. The reflection loss (RL) was calculated with the following equation [19,20]:

$$Z_{in} = Z_0 \cdot \sqrt{\frac{\mu_r}{\varepsilon_r}} \tanh\left[j \cdot \frac{2\pi f d}{c} \sqrt{\mu_r \cdot \varepsilon_r}\right] \tag{5}$$

$$RL = 20\lg\left|\frac{Z_{in} - Z_0}{Z_{in} + Z_0}\right| \tag{6}$$

where $\varepsilon_r$, $\mu_r$, $Z_{in}$, and $Z_0$ are the complex permittivity, the complex permeability, the input characteristic impedance, and the free space impedance, respectively. $c$, $d$, and $f$ are the light velocity in vacuum, the thickness, and the testing frequency, respectively. The attenuation constant ($\alpha$), which defines the absorption property, can be calculated using the equation:

$$\alpha = \frac{\sqrt{2}\pi f}{c} \times \sqrt{(\mu''\varepsilon'' - \mu'\varepsilon') + \sqrt{(\mu''\varepsilon'' - \mu'\varepsilon')^2 + (\mu''\varepsilon' - \mu'\varepsilon'')^2}} \tag{7}$$

## 3. Results and discussion

### 3.1. *Detoxification of distillation residue*

Pulsed joule heating was performed using a tube reactor (Fig. 2a). The temperature is primarily influenced by the pulse voltage, duration and the reactant resistance. The initial discharge removes the volatiles of the raw material, reduces its resistance, and sets the stage for the subsequent heating process. The photo during the actual reaction process is shown in the Fig. 2b and Fig. S4. The heat is generated directly within the feedstock, eliminating slow and inefficient heat transfer that traditional tube furnaces experience. Extending the pulse duration can increase the maximum achievable temperature in the reaction, potentially reaching 1800–3000 °C, with a heating rate of 400–850 °C/s and a cooling rate of 80–250 °C/s (Fig. 2c).

Fig. 2d compares the chromatograms of the original distillation residue and tPG-10 s extracted by hexane. It can be observed that the DR contains a variety of high-concentration chlorinated pollutants, among which HCBD has the highest peak area, followed by pentachlorobenzene and octachlorostyrene, as well as other chlorinated pollutants such as 1,1,3,3,4,4-hexachloro-1-butene, 1,1,2,3,3-pentachloropropane and hexachlorobenzene (Table S4). After pulsed Joule heating for 10 s, all the peaks of chlorinated pollutants disappeared, indicating an outstanding detoxification performance of PJH on DR. For example, the raw concentration of HCBD of DR reached 5580 mg/kg. As shown in Fig. 2e, the removal of pollutants was influenced by the discharge time of the second pulse. As the discharge time extends from 1 s to 10 s, the removal of HCBD improved from 17.3 % to 99.1 %. The energy consumption during different PJH processes was calculated based on the integral of real-time power curves (Fig. S5). The results are shown in Fig. 2f. As the pulse time extended from 1 s to 10 s, the energy consumption increased from 9.1 kJ/g to 69.9 kJ/g. Note that the energy consumption nearly doubled when the time increased from 7.5 s to 10 s, while the removal of HCBD had already exceeded 90 % at 5 s discharge. As shown in Fig. 2g, the efficacy (pollutant degraded per unit of energy consumption) reached the highest (187.3 mg/kJ) at the discharge time of 5 s, indicating the most economic choice for electrothermal remediation. In addition, owing to the fast heating rate and high peak temperature, PJH-based remediation demonstrates significant advantages in treating hazardous wastes with high concentration of persistent organic pollutants. As shown in Fig. 2g, PJH outperforms traditional methods for chlorinated organic pollutants remediation, offering shorter processing time and higher degradation efficiency (Table S5). Furthermore, the emitted organic pollutants were captured by adsorption tube and analyzed through GC-MS. Results showed that chloroethylene (peak 4, 7, 12, 14) was the main chlorinated byproduct in gas phase (Fig. S8). Alkaline additives are suggested to facilitate the dichlorination reactions to control the toxic pollutant emission. Additionally, to explore the chlorine migration characteristics, the distribution of chlorine at different heating time was also tested and shown in Fig. S10. As the PJH time increased from 1 to 10 s, the solid-phase organic chlorine gradually decreased from 40 % to 3 %. In contrast, the total inorganic chlorine (solid phase + gas phase) increased from 3 % to 50 %, primarily due to the cleavage of the C-Cl bond in DR, where Cl reacts with a proton (H) to form HCl. However, due to the limited hydrogen in raw DR (0.31 %), more hydrogen or alkaline additives are suggested to supplement for complete dichlorination in future studies.

### 3.2. *Characterization of PJH products*

Flash Joule heating has been reported for graphene synthesis from carbon enriched solid wastes. To identify the PJH products, Raman spectroscopy, as a common technique for graphene characterization [21], was employed for tPG-10 s. The result is shown in Fig. 3a. This spectrum displayed distinct peaks: D peak at 1350 $cm^{-1}$, G peak at 1580 $cm^{-1}$, and 2D peak at 2700 $cm^{-1}$, respectively. The ratio of the intensity of D peak ($I_D$) and G ($I_G$) peak indicates the defect density in the carbon materials [22]. For tPG-10 s, the $I_D/I_G$ is 0.075, signifying a low defect density. Additionally, the intensity ratio of 2D peak to G peak is 2.12. The high $I_{2D}/I_G$ ratio suggests minimal interlayer optical coupling in the tPG-10 s [36]. Furthermore, in the inset of Fig. 3a, two additional peaks at 1863 $cm^{-1}$ and 2035 $cm^{-1}$ are observed, which could be attributed to the turbostratic peaks of graphene (TS1 and TS2). These peaks indicate a rotationally disordered arrangement of the graphene layers, differing from the traditional AB-stacked mode in tPG-10 s. This characteristic imparts excellent exfoliation efficiency of the graphitic products in solvent, which is advantageous for the synthesis of graphene-based composites.

As the pulse time increased, the Raman spectrum of the tPG exhibited

**Table 1**

Proximate and ultimate analyses of the distillation residue.

| Proximate analysis (wt%) | | | | Ultimate analysis (wt%, daf) | | | | | | $Q_b$ (MJ/kg) |
|---|---|---|---|---|---|---|---|---|---|---|
| $M_{ad}$ | $V_{ad}$ | $FC_{ad}$ | $A_{ad}$ | C | H | N | S | Cl | O* | 13.22 |
| 3.91 | 61.69 | 29.7 | 4.7 | 39.75 | 0.31 | 0.04 | 0.38 | 28.74 | 22.17 | |

Note: ad, air dried basis; *, by difference an increase in the $I_{2D}/I_G$ ratio from 0.20 to 2.1, and a decrease in the $I_D/I_G$ ratio from 1.7 to 0.075 (Fig. 3b and Fig. S10a). These changes suggest that extending the pulse time enhances the quality of the graphene products, likely due to the elevated peak temperatures shown in Fig. 2c. Moreover, Raman spectrum of the initial raw distillation residue indicated that the structure was amorphous carbon (Fig. S10b).

TGA in air atmosphere further confirmed the conversion of the distillation residue feedstock from amorphous carbon to graphitic carbon (Fig. 3c). The initial distillation residue started to degrade at approximately 150 °C and was completely degraded by around 650 °C. After PJH, the weight loss of the treated products starts at a temperature over 400 °C. Moreover, as the pulse time extend from 1 s to 10 s, the onset temperature of the weight loss increased from 400 to 650 °C. The high thermal stability of tPG indicates a significant degree of crystallinity and low defect concentrations, as defects typically reduces the thermal stability of graphene [23]. The elevated onset temperature demonstrates that the thermal stability of the product was enhanced and that the degree of graphitization gradually improved as the pulse time increased [24]. This trend is corroborated by the Raman spectra. The proximate analysis of the initial DR under study indicates an ash content of 4.7 wt%. The very low ash content in the DR ensures the stability of the discharge current during the Joule thermal process and contributes to the production of high-quality graphene that is readily applicable in microwave absorption.

XRD patterns of DR and tPG-10 s are shown in Fig. 3d. A broad peak between 15° and 35° (with a peak position at 24.3°) is detected on raw DR, confirming its amorphous carbon structure [25]. In contrast, the dominant (002) peak of the tPG appears at 26.1°, which is a lower diffraction angle compared to graphite (26.6°) and has a wider full width at half maximum (FWHM), indicating the successful graphitization of the DR [25]. According to Bragg's law, the average lattice spacing of tPG-10 s is 0.35 nm, larger than that of the AB-stacked graphene (0.335 nm)[26]. Additionally, this peak has a tail extending to lower 2θ values, indicating rotational disordered arrangement of the graphene layers [12]. Furthermore, the intensity of the three-dimensional (3D) peaks at (101) 43.1° and (102) 53.7° are lower than that of graphite, suggesting a turbulent or vortex-like structure [27]. These results confirm the presence of turbostratic graphene structure in derived tPG-10 s [11], consistent with the TS1 and TS2 peaks in Raman spectrum (Fig. 3a).

XPS was conducted to determine the surface chemistry of the materials (Fig. 3e). Results revealed that the surface carbon content increased from 89.76 % in the distillation residue to 96.44 % in the tPG-10 s after the PJH. The initial DR raw material contained heteroatoms such as oxygen and chlorine. However, the PJH process significantly reduced the content of these heteroatoms. The survey spectrum (Fig. 3e)

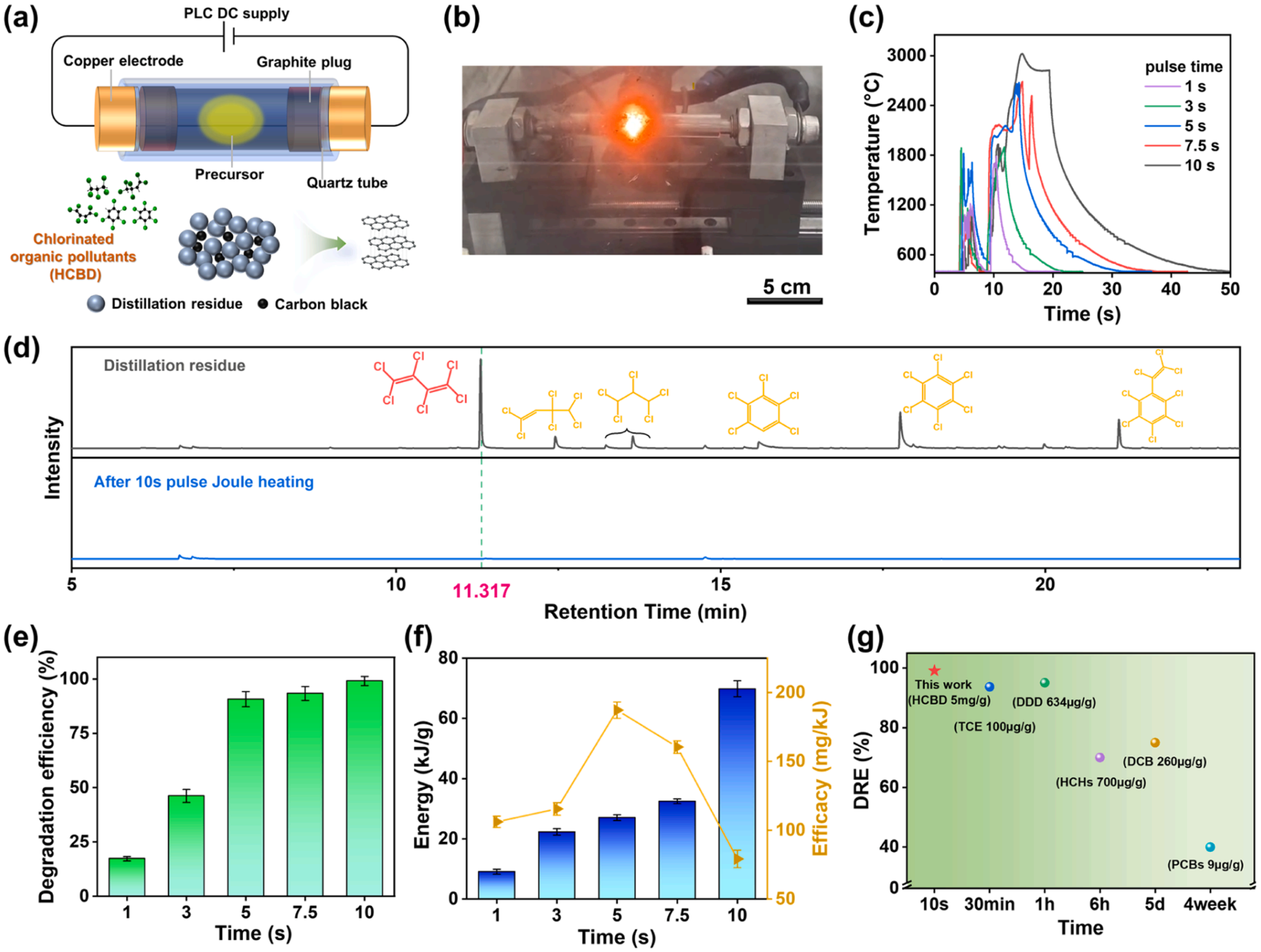

**Fig. 2.** Detoxification of HCBD polluted distillation residue. (a) Schematic diagram of the experimental setup and process. (b) Digital photo of the sample during heating process. (c) The temperature profile of PJH over the course of the reaction. (d) GC-MS spectra of raw and treated DR. (e) effect of pulse time on the HCBD degradation efficiency. (f) Energy consumption and efficacy of PJH with varying pulse durations. (g) Comparison of different methods for degradation of highly chlorinated contaminated solids. All error bars represent standard deviation.

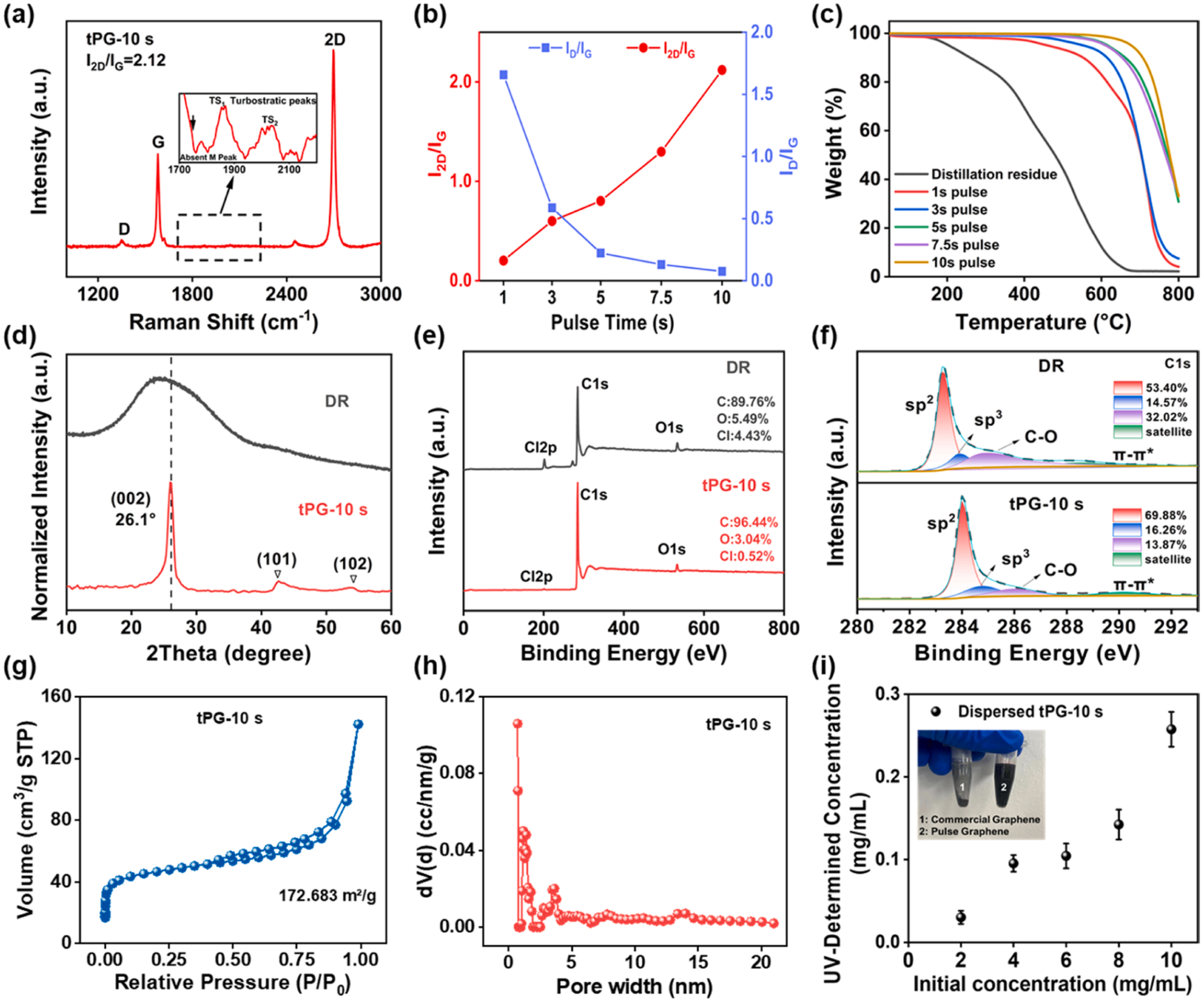

**Fig. 3.** Characterization of tPG derived from distillation residue. (a)Raman spectrum of tPG-10 s, (b) Effect of discharge time on $I_D/I_G$ ratio and $I_{2D}/I_G$ ratio derived from raman spectra, (c) TGA curves of distillation residues and tPGs under air atmosphere, (d) XRD patterns (e) XPS survey spectrum, and (f) High-resolution XPS spectra of C1s of the distillation residues and tPG-10 s, (g) $N_2$ adsorption-desorption isotherms, (h) Pore size distribution of tPG-10 s, (i) UV–vis dispersion map of tPG-10 s concentration compared to commercial graphene.

showed that the surface oxygen content decreased from ~5.49 % to ~3.04 %, while the surface chlorine content decreased from ~4.43 % to near-zero. XPS analysis further confirmed that impurities were removed through the PJH process, as the intensity of the Cl peak in the graphene products was significantly reduced compared to the distillation residue (Fig. 3e). The Cl 2p of DR and tPG-10 s are shown in Fig. S11. Organic-chlorine constituted over 90 % in the raw DR, after PJH, the signal of Cl 2p became undetectable, indicating that the organic-chlorine in raw DR was broken down and emitted from the solid phase during PJH. Further, the high-resolution C1s spectrum of the distillation residue (Fig. 3f) can be deconvolved into four components centered at ~284.0 eV, ~284.8 eV, ~286.6 eV, and ~290.5 eV, corresponding to C═C, C-C, C-O, and the satellite peak of π-π* bond, respectively. Moreover, the π-π* transition is evident at 290.5 eV. After the PJH reaction, the proportion of the $sp^2$ band increased from 53.4 % to 69.9 %, and the intensity of the $sp^3$ band decreased. These findings confirm the conversion of the amorphous carbon to $sp^2$ hybrid graphitic carbon [28].

The surface area of the tPG was characterized using the Brunauer-Emmett-Teller (BET) gas adsorption method. $N_2$ physical adsorption was employed to determine the specific surface area, pore volume, and pore size distribution of the tPG-10 s. The results are shown in Fig. 3g, h and Fig. S12. The specific surface area was calculated using the BET method, and the pore volume and pore size distribution were obtained using the Density Functional Theory (DFT) method. The BET analysis demonstrated a specific surface area of 172.7 $m^2/g$ and a cumulative pore volume of 0.14 $cm^3$ /g with a mesoporous structure.

UV–vis spectroscopy was employed to analyze the exfoliation and dispersion of the tPG in the solvent, which are crucial characteristics for the successful application of the tPG in composite materials. As shown in Fig. 3i, the dispersibility of the tPG-10 s was tested in 1 % Pluronic-127, a surfactant. The dispersion of the tPG is significantly superior to that of commercially synthesized graphene produced by physical exfoliation methods (inner images in Fig. 3i), where the solutions remained stable and well-dispersed even after 1 month of storage. The concentration of tPG-10 s is 0.03 mg/mL at a dose of 2 g/L, and at a dose of 10 g/L, it can reach 0.26 mg/mL, which is higher than that of graphene derived from the municipal solid waste and metallurgical coke [29,30].

SEM-EDS mapping was employed to visualize the morphology and structure of the DR and the tPG, as depicted in Fig. 4a-h. The distillation residue exhibited a smooth and regular square-like shape, whereas the

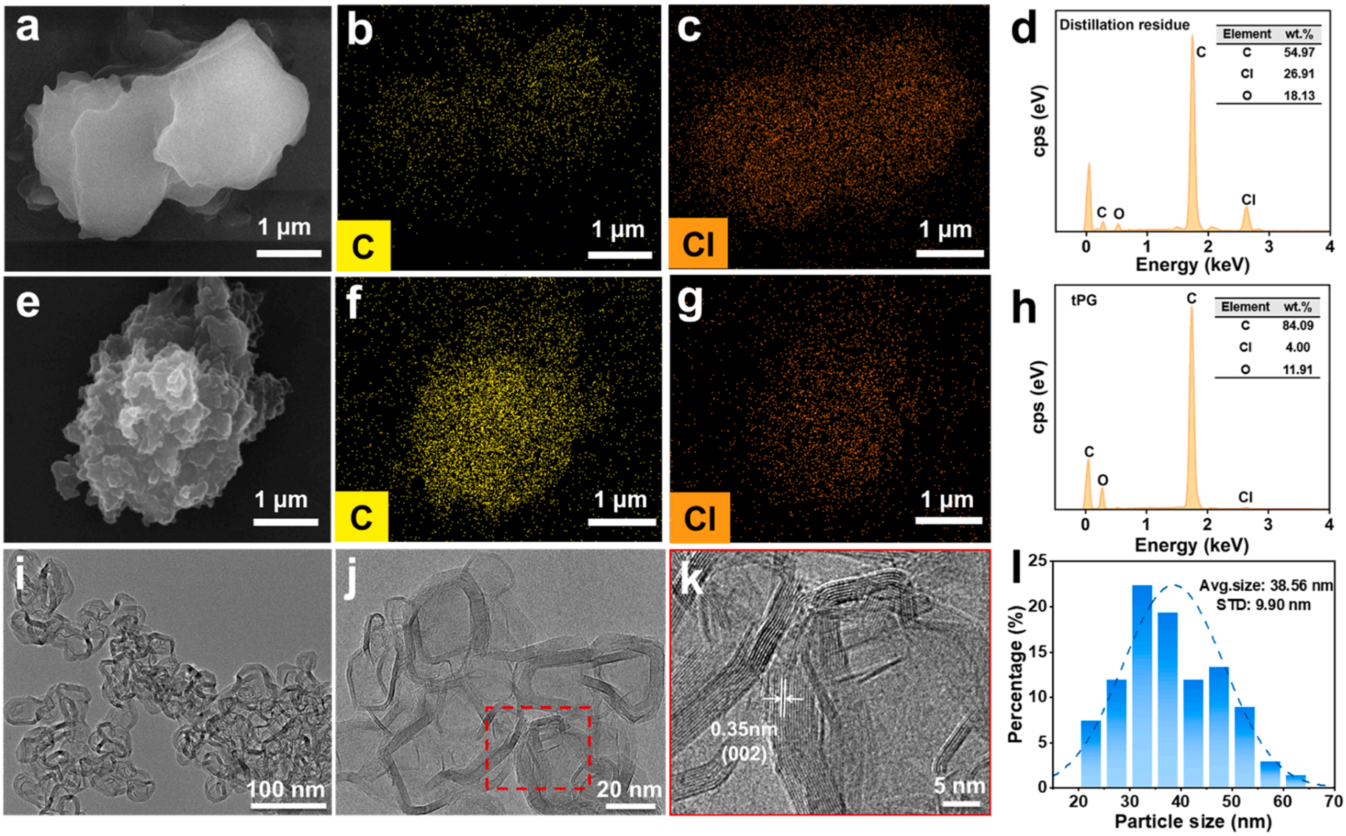

**Fig. 4.** Morphologies of DR and tPG-10 s (a-d) SEM-EDS mapping of DR, (e-f) SEM-EDS mapping of tPG, (i-k) TEM image of the tPG-10 s, (l) Lateral size distribution obtained by TEM image analysis techniques of the Feret diameter.

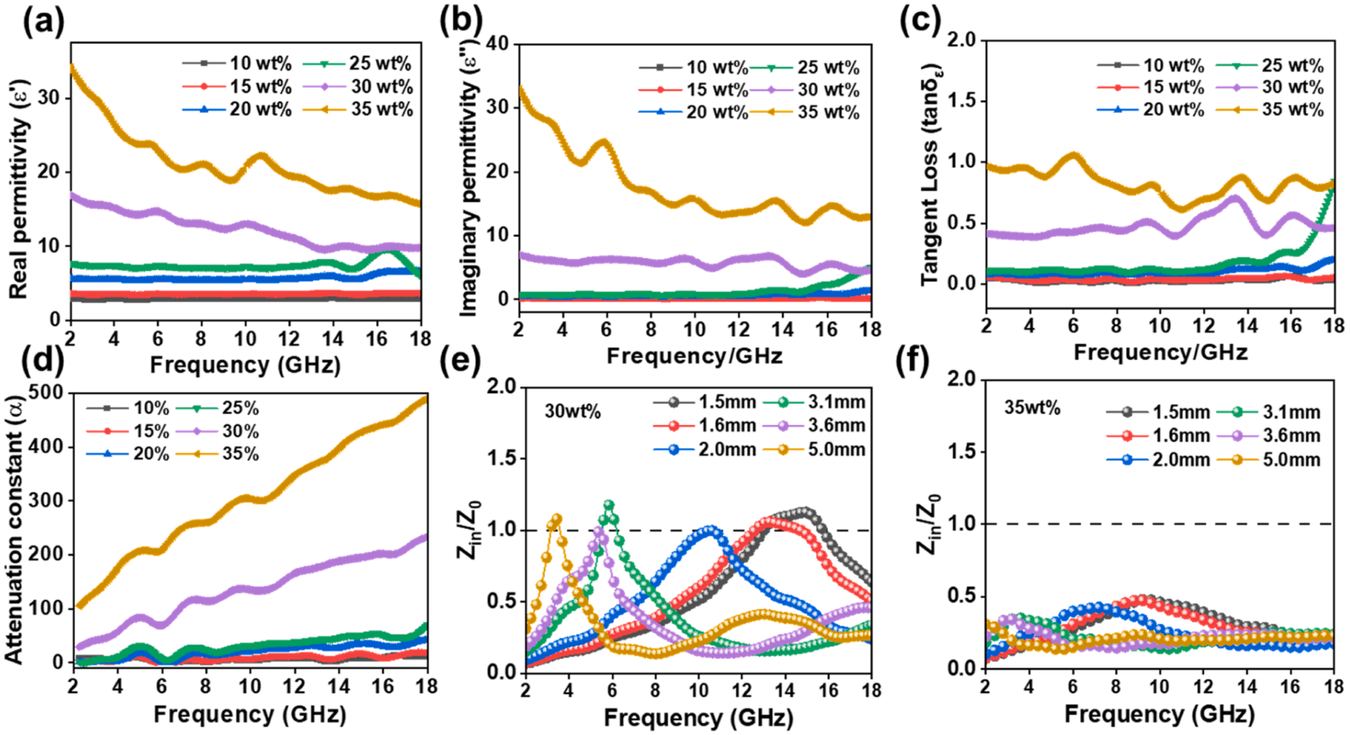

**Fig. 5.** (a–b) Real (ε′) and imaginary (ε″) parts of the complex permittivity for tPG, (c) Dielectric loss tangent (tanδ$_\varepsilon$), (d) Attenuation constant of tPG with loading of 30 wt%, (e-f) Impedance-f curves with loading of 30 wt% and 35 wt%.

tPG displayed a folded, stacked, and highly crystalline sheet-like morphology. The particle size changed minimally before and after the reaction, with an average transverse size of approximately 4 μm. EDS and elemental mapping analyses revealed that the proportion of surface carbon increased significantly from 55.0 % to 84.1 % after the PJH reaction, while the proportions of the impurity elements chlorine and oxygen decreased from 26.9 % and 18.1–4.0 % and 11.9 %, respectively. Transmission electron microscopy (TEM) images in Fig. 4i revealed a uniform graphene nanoplates of tPG-10 s. The two-dimensional (2D) and few-layered structure could be observed in Fig. 4j. A lattice space of 0.350 nm was estimated in Fig. 4k, which is consistent with the (002) peak position in XRD pattern (Fig. 3d). As depicted in Fig. 4l, the estimated average transverse size of the tPG nanoplates is approximately 38.56 nm, with a standard deviation of 9.90 nm. According to statistics, the Feret diameter of tPG nanoplates is predominantly concentrated in the range of 30–40 nm, accounting for 41.8 % of the distribution. All sheet sizes fall within the range of greater than 20 nm and less than 70 nm. The nanoscale size and large lattice spacing endow the tPG an excellent dispersibility and high exfoliation efficiency during composite fabrication.

### 3.3. *Electromagnetic wave absorbing performance of tPG*

To explore potential applications for the tPG produced from distillation residue, tPG/paraffin composites were prepared as described previously. Fig. 5a-c present the EM parameters ($\varepsilon'$ and $\varepsilon''$) and dielectric loss tangent ($\tan\delta_\varepsilon = \varepsilon''/\varepsilon'$) for samples with varying tPG-10 s filling contents in the frequency range of 2–18 GHz. Generally, the electromagnetic absorbing behavior of tPG, which lacks magnetic components, is attributed to dielectric loss. The values of the real ($\varepsilon'$) and imaginary ($\varepsilon''$) parts of the complex permittivity ($\varepsilon_r = \varepsilon'\text{-}j\varepsilon''$) determine the EMW absorption characteristics of designed absorbers, which are related to storage and dissipation capacity, respectively [31].

For samples with 30 wt% and 35 wt% tPG filling contents, the $\varepsilon'$ value decreases with increasing frequency, ranging from 16.93 to 9.82 and 34.27–15.66, respectively. As the frequency increases, the complex permittivity varies depending on the specific material type. In graphene materials, both high crystallinity and high carbon content significantly enhance electrical conductivity. This trend in $\varepsilon'$ value across the tested frequency range is consistent with the dispersion phenomenon of carbon materials [32]. As depicted in Fig. 5b, for the samples with 30 wt% and 35 wt% tPG filling, the $\varepsilon''$ value also decreased with increasing frequency, ranging from 7.00 to 3.99 and 33.01–12.04, respectively. Moreover, when tPG content is lower than 25 %, both $\varepsilon'$ and $\varepsilon''$ values were less than 10 and 2, respectively, indicating minimal EMW absorbing capacity. This is attributed to the insufficient filling amount of tPG, which prevents the formation of a complete conductive network. These results demonstrate that the $\varepsilon'$ and $\varepsilon''$ value increase significantly with the mass percentage of tPG in the sample, confirming that a higher amount of tPG sheets enhances dipolar polarization and electrical conductivity. Additionally, the ε' and ε'' curve graph and tangent loss of high content tPG exhibit multiple fluctuation peaks, which can be attributed to the skin effect of the material and its high conductivity [33]. The fluctuation of the curve here is due to the existence of multiple relaxation processes including defect polarization relaxation and groups' electronic dipole relaxation. These various mechanisms contribute to the overall dielectric response, leading to the observed variations in performance.

Their dielectric loss tangent ($\tan\delta_\varepsilon = \varepsilon''/\varepsilon'$) also indicates that the tPG exhibit the steadily upward trend when the filling ratio increases from 10 to 35 wt% (Fig. 5c), implying an improvement in their dielectric loss capacity [31]. Furthermore, the attenuation coefficient ($\alpha$) of the carbon-based sample represents the loss of EMW intensity as it propagates through the material [34] (Fig. 5d). The trend of $\alpha$ is consistent with the EMW absorbing capacity.

In addition to the intrinsic microwave attenuation characteristics, matching the characteristic impedance is also crucial for effective EMW attenuation [35]. The impedance matching value ($Z = |Z_{in}/Z_0|$) should approach 1, indicating that more EMWs can enter the absorbers; otherwise, EMWs are reflected from the surface of the material [36,37]. Fig. 5e and f show the impedance matching diagrams for the samples with 30 wt% and 35 wt% tPG addition. Specifically, the impedance matching Z value for the 30 wt% sample is close to 1, with a specific variation range of 0.998–1.176. In contrast, the impedance matching Z variation range for the 35 wt% sample is 0.308–0.479, which is significantly less than 1 within the same absorbing layer thickness range. It is noteworthy that, although the complex permittivity of the 35 wt% tPG sample is higher than that of other samples, the excessively high parameters result in impedance mismatch and suboptimal EMW absorption performance [38].

To reveal their EMW absorption performances, the reflection loss (RL) curves were calculated using Eqs. (3) and (4). Fig. 6a shows the RL versus frequency curve of the 30 wt% tPG sample at various thicknesses. Effective absorption of −10 dB (90 % electromagnetic wave absorption) [39] can be achieved at all given thicknesses. The maximum effective absorption bandwidth ($EAB_{max}$) reaches 3.9 (12.8~ 16.7 GHz), nearly covering the entire Ku band (12~ 18 GHz). At the sample thickness of 1.6 mm, $RL_{min}$ can reach as low as −42.0 dB (99.994 % wave absorption) at a corresponding frequency position of 14.48 GHz. Compared to the previously reported results, this material performs favorably, even surpassing that of some MXene-based materials [40,41]. Furthermore, the $RL_{min}$ shifts towards lower frequencies with increasing material thickness, which is attributed to the quarter-wavelength resonant interfering attenuation mechanism of the EMW absorption material on the surface [42].

As illustrated in Fig. 6b, the 3D RL color maps reveal that the performance of the 30 wt% tPG/paraffin composites as a function of thickness and frequency. The performance data for the other samples is provided in Fig. S14. Besides, Fig. 6c presents the 2D color-coded contour plots of reflection loss values. The effective absorption bandwidth of the tPG/paraffin nanocomposite exceeds 3 GHz, primarily distributed between 1.5 mm and 2.2 mm in thickness. Additionally, the tPG can acquire the maximum area marked by black bold lines, where the RL values are below −10 dB.

Comparatively, Fig. 6d-f shows that the $RL_{min}$ of the sample with 35 wt% tPG addition is significantly lower than that for the 30 wt% sample. This indicates the necessity to screen for a "moderate" dielectric property in practical applications. Moreover, it is evident that the very low electromagnetic parameters with low tPG additions (below 30 wt%) result in poor EMW absorption performance (Fig. S14).

In addition to excellent electromagnetic absorption performance, thickness is also a crucial indicator for evaluating the EMW absorbing materials in practical applications [40,41]. Graphene and its derivatives have shown potential for EMW absorption, but their performance has not been as impressive as expected. This is primarily attributed to their relatively high complex dielectric constant and sole dielectric relaxation process, which negatively impacts the matching of the characteristic impedance. Compared to recently reported graphene-based EMW absorbing materials [43], remarkably, the tPG composite material demonstrates a superior advantage in both reflection loss and thickness, indicating its broad application potential as advanced EMW absorbing materials (Fig. 6g). The excellent wave absorption performance of tPG can be attributed to the structural characteristics: moderate graphitization, thin lamellae, porous structure, and effective dispersion within the matrix. It is also the result of effective impedance matching, attenuation capabilities, and interference loss. Moreover, they are cost-effective, stable, and characterized by a straightforward manufacturing process.

Fig. 6h shows a schematic diagram of the EMW absorption mechanism for tPG. Since tPG does not contain magnetic components, polarization loss and conduction loss are the primary mechanisms by which conductive electromagnetic absorbers achieve energy attenuation [44,

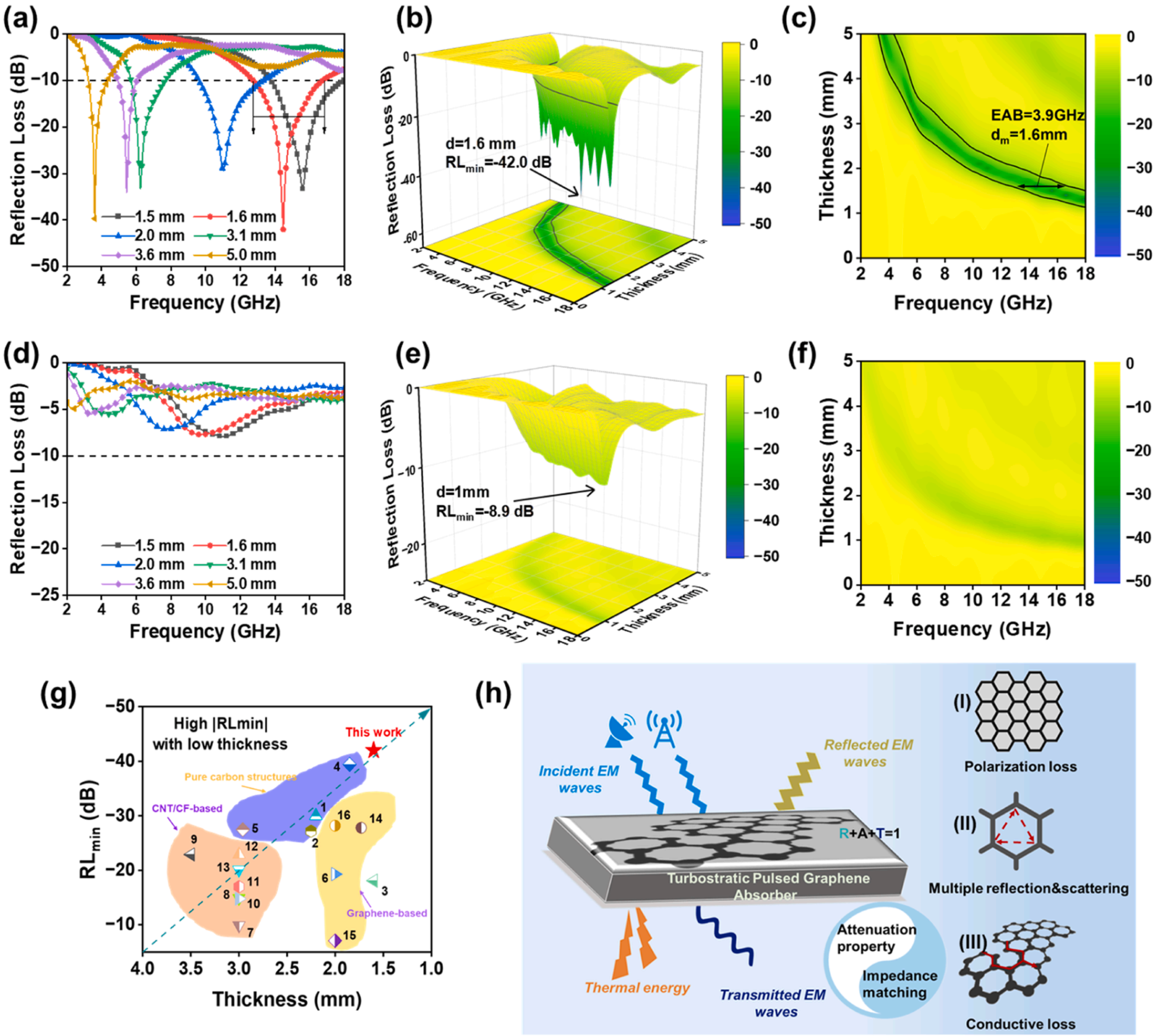

**Fig. 6.** (a) RL-f at different thicknesses, (b) three-dimensional RL−f curves and (c) its corresponding 2D contour maps with loading of 30 wt% tPG, (d) RL-f at different thicknesses, (e) three-dimensional RL−f curves and (f) its corresponding 2D contour maps with loading of 35 wt% tPG, (g) Comparison of the EMW absorption performance in view of RL$_{min}$, and matching thickness with reported Carbon-based nanomaterials as EMW absorption materials, which are listed in Table S6, (h) Schematic illustration of the EMW absorption mechanisms for tPG absorber.

45]. To further verify the absorption loss mechanism, the Cole-Cole curve of tPG is plotted according to the Debye relaxation theory (Eqs. S1–3), as shown in Fig. S15 [46]. Generally, the semicircle and the approximate linear segment correspond to polarization loss and conduction loss, respectively [47]. Additionally, multiple reflections and scatterings of EMW play a critical role in its absorber attenuation, especially for turbostratic-stack graphene[34].

In summary, the abundance of C═C bonds in the graphite nanocrystals forms a two-dimensional plane, thereby reducing the electrical resistivity [37]. The Raman spectroscopy results align with the findings from the XRD and XPS analyses described above. SEM and TEM studies show that the obtained tPGs all exhibit a representative turbostratic-stacked nanosheet heterostructure. Furthermore, the porous structure improves EMW absorption by increasing multiple reflections and interface polarization, thereby enhancing the dielectric loss. Moreover, the tPG with a three-dimensional turbulent structure constructs a good conductive network, provides abundant air-solid interfaces, and promotes multiple scattering, reflection, and attenuation of EMW [48]. Collectively, these unique tPG heterostructures significantly optimize impedance matching performance and increase dielectric loss capability, resulting in excellent EMW absorption performance.

## 4. Conclusion

In this work, a pulse Joule heating (PJH) method was designed for managing distillation residues contaminated with high concentrations of HCBD. This approach not only effectively degrades these pollutants, but also rapidly produces graphene-based absorbing materials, achieving the "two-in-one" effect. The degradation efficiency of high-concentration HCBD has reached over 90 % and 99 % after 5 s and 10 s of pulsed discharge, respectively. From an economic perspective, the HCBD degraded (mg) per energy consumption (kJ) reached the highest (187.3 mg/kJ) with a 5 s discharge time. Product characterization results confirmed the direct synthesis of high-quality graphene with a distinctive turbulent morphology via PJH, thus streamlining the process and offering economic benefits. The DR derived graphene was then successfully utilized as an EMW absorbing material, achieving an effective absorption bandwidth of 3.9 GHz and a reflection loss of −42.0 dB with a low matching thickness of 1.6 mm at 30 wt% filling content. This work highlights the significant potential for upcycling hazardous waste into advanced microwave absorption applications.

## CRediT authorship contribution statement

**Tong Chen:** Writing – review & editing, Writing – original draft, Supervision, Funding acquisition, Conceptualization. **Yunxiao Zhao:** Writing – original draft, Visualization, Formal analysis, Data curation. **Hanyang Sun:** Visualization, Methodology, Investigation. **Xinyu Niu:** Methodology, Investigation, Data curation. **Pei Li:** Writing – review & editing, Supervision, Resources, Conceptualization. **Yan Xia:** Writing – review & editing, Supervision, Investigation, Funding acquisition, Data curation. **Xiaoqing Lin:** Writing – review & editing, Supervision, Resources, Methodology, Investigation. **Xiaodong Li:** Writing – review & editing, Supervision. **Ying Wang:** Supervision, Resources, Methodology. **Jianhua Yan:** Supervision, Resources. **Chen Sun:** Writing – review & editing, Supervision, Resources, Funding acquisition, Conceptualization.

## Declaration of Competing Interest

The authors declare that they have no known competing financial interests or personal relationships that could have appeared to influence the work reported in this paper.

## Acknowledgements

This study is supported by the National Science Foundation of China (No.52306280 and No.523B2065), "Lingyan" Research and Development Project of Zhejiang Province (2024C03232), and the Research Funds of Institute of Zhejiang University-Quzhou (IZQRCZX023 and IZQ2023KJ1001).

## Appendix A. Supporting information

Supplementary data associated with this article can be found in the online version at doi:10.1016/j.jhazmat.2025.137160.

## Data availability

Data will be made available on request.

## References

[1] UNEP, 2015. Report of the Conference of the Parties to the Stockholm Convention on Persistent Organic Pollutants on the Work of Its Seventh Meeting, UNEP/ POPS/ COP.7/36, 23 June.

[2] UNEP, 2017. Report of the Conference of the Parties to the Stockholm Convention on Persistent Organic Pollutants on the Work of Its Eighth Meeting, UNEP/ POPS/ COP.8/32, 13 July.

[3] List of New Pollutants under Priority Control (2023 Edition) Ministry of Ecology and Environment of the People's Republic of China. ⟨https://www.mee.gov.cn/gzk/gz/202212/t20221230_1009192.shtml⟩.

[4] UNEP, 2017. Technical Guidelines on the Environmentally Sound Management of Wastes Consisting of, Containing or Contaminated with Hexachlorobutadiene.

[5] Kajiwara, N., Noma, Y., Matsukami, H., Tamiya, M., Koyama, T., Terai, T., Koiwa, M., Sakai, S., 2019. Environmentally sound destruction of hexachlorobutadiene during waste incineration in commercial- and pilot-scale rotary kilns. J Environ Chem Eng 7, 103464. https://doi.org/10.1016/j.jece.2019.103464.

[6] Zhang, H., Wang, Y., Sun, C., Yu, M., Gao, Y., Wang, T., Liu, J., Jiang, G., 2014. Levels and distributions of hexachlorobutadiene and three chlorobenzenes in biosolids from wastewater treatment plants and in soils within and surrounding a chemical plant in China. Environ Sci Technol 48, 1525–1531. https://doi.org/10.1021/es405171t.

[7] X. Lu, 2015. Study of production pollution characteristics and biotoxicity of benzene series products distillation residues, Master, Beijing University of Chemical Technology.

[8] Yao, L., 2022. Analysis on production and consumption status and market prospects of trichloroethylene. Chlor Alkali Ind 58, 15–20. https://doi.org/10.3969/j.issn.1008-133X.2022.09.005.

[9] Cai, P., Fu, J., Zhan, M., Jiao, W., Chen, T., Li, X., 2022. Formation mechanism and influencing factors of dioxins during incineration of mineralized refuse. J Clean Prod 342, 130762. https://doi.org/10.1016/j.jclepro.2022.130762.

[10] Luong, D.X., Bets, K.V., Algozeeb, W.A., Stanford, M.G., Kittrell, C., Chen, W., Salvatierra, R.V., Ren, M., McHugh, E.A., Advincula, P.A., Wang, Z., Bhatt, M., Guo, H., Mancevski, V., Shahsavari, R., Yakobson, B.I., Tour, J.M., 2020. Gram-scale bottom-up flash graphene synthesis. Nature 577, 647–651. https://doi.org/10.1038/s41586-020-1938-0.

[11] Advincula, P.A., Luong, D.X., Chen, W., Raghuraman, S., Shahsavari, R., Tour, J. M., 2021. Flash graphene from rubber waste. Carbon 178, 649–656. https://doi.org/10.1016/j.carbon.2021.03.020.

[12] Algozeeb, W.A., Savas, P.E., Luong, D.X., Chen, W., Kittrell, C., Bhat, M., Shahsavari, R., Tour, J.M., 2020. Flash graphene from plastic waste. ACS Nano 14, 15595–15604. https://doi.org/10.1021/acsnano.0c06328.

[13] Deng, B., Luong, D.X., Wang, Z., Kittrell, C., McHugh, E.A., Tour, J.M., 2021. Urban mining by flash Joule heating. Nat Commun 12, 5794. https://doi.org/10.1038/s41467-021-26038-9.

[14] Deng, B., Carter, R.A., Cheng, Y., Liu, Y., Eddy, L., Wyss, K.M., Ucak-Astarlioglu, M. G., Luong, D.X., Gao, X., JeBailey, K., Kittrell, C., Xu, S., Jana, D., Torres, M.A., Braam, J., Tour, J.M., 2023. High-temperature electrothermal remediation of multi-pollutants in soil, 6371–6371 Nat Commun 14. https://doi.org/10.1038/s41467-023-41898-z.

[15] Advincula, P.A., Meng, W., Eddy, L.J., Scotland, P.Z., Beckham, J.L., Nagarajaiah, S., Tour, J.M., 2024. Replacement of concrete aggregates with coal-derived flash graphene. ACS Appl Mater Interfaces 16, 1474–1481. https://doi.org/10.1021/acsami.3c15156.

[16] Advincula, P.A., Granja, V., Wyss, K.M., Algozeeb, W.A., Chen, W., Beckham, J.L., Luong, D.X., Higgs, C.F., Tour, J.M., 2023. Waste plastic- and coke-derived flash graphene as lubricant additives. Carbon 203, 876–885. https://doi.org/10.1016/j.carbon.2022.12.035.

[17] S.A.C. Aqsio, GB/T 212-2008, Proximate Analysis of Coal, Standards Press of China: Beijing, 2008.

[18] S.A.C. Aqsio, GB/T 31391-2015, Ultimate analysis of coal Standards Press of China: Beijing, 2015.

[19] Naito, Y., Suetake, K., 1971. Application of ferrite to electromagnetic wave absorber and its characteristics. IEEE Trans Micro Theory Tech 19, 65–72. https://doi.org/10.1109/TMTT.1971.1127446.

[20] Kim, S.S., Jo, S.B., Gueon, K.I., Choi, K.K., Kim, J.M., Churn, K.S., 1991. Complex permeability and permittivity and microwave absorption of ferrite-rubber composite at X-band frequencies. IEEE Trans Magn 27, 5462–5464. https://doi.org/10.1109/20.278872.

[21] Wu, J.-B., Lin, M.-L., Cong, X., Liu, H.-N., Tan, P.-H., 2018. Raman spectroscopy of graphene-based materials and its applications in related devices. Chem Soc Rev 47, 1822–1873. https://doi.org/10.1039/C6CS00915H.

[22] Wang, Q., Liu, F., Jin, Z., Qiao, X., Huang, H., Chu, X., Xiong, D., Zhang, H., Liu, Y., Yang, W., 2020. Hierarchically divacancy defect building dual-activated porous carbon fibers for high-performance energy-storage devices. Adv Funct Mater 30, 2002580. https://doi.org/10.1002/adfm.202002580.

[23] Sádovská, G., Honcová, P., Morávková, J., Jirka, I., Vorokhta, M., Pilař, R., Rathouský, J., Kaucký, D., Mikysková, E., Sazama, P., 2023. The thermal stability of carbon materials in the air: quantitative structural investigation of thermal stability of carbon materials in air. Carbon 206, 211–225. https://doi.org/10.1016/j.carbon.2023.02.042.

[24] Saadi, M.A.S.R., Advincula, P.A., Thakur, M.S.H., Khater, A.Z., Saad, S., Shayesteh Zeraati, A., Nabil, S.K., Zinke, A., Roy, S., Lou, M., Bheemasetti, S.N., Bari, M.A.A., Zheng, Y., Beckham, J.L., Gadhamshetty, V., Vashisth, A., Kibria, M.G., Tour, J.M., Ajayan, P.M., Rahman, M.M., 2022. Sustainable valorization of asphaltenes via flash Joule heating. Sci Adv 8, eadd3555. https://doi.org/10.1126/sciadv.add3555.

[25] Wyss, K.M., De Kleine, R.D., Couvreur, R.L., Kiziltas, A., Mielewski, D.F., Tour, J. M., 2022. Upcycling end-of-life vehicle waste plastic into flash graphene. Commun Eng 1, 3. https://doi.org/10.1038/s44172-022-00006-7.

[26] Pope, C.G., 1997. X-ray diffraction and the Bragg equation. J Chem Educ 74, 129. https://doi.org/10.1021/ed074p129.

[27] Li, Z.Q., Lu, C.J., Xia, Z.P., Zhou, Y., Luo, Z., 2007. X-ray diffraction patterns of graphite and turbostratic carbon. Carbon 45, 1686–1695.

[28] Zhu, X., Lin, L., Pang, M., Jia, C., Xia, L., Shi, G., Zhang, S., Lu, Y., Sun, L., Yu, F., Gao, J., He, Z., Wu, X., Li, A., Wang, L., Wang, M., Cao, K., Fu, W., Chen, H., Li, G., Zhang, J., Wang, Y., Yang, Y., Zhu, Y.-G., 2024. Continuous and low-carbon production of biomass flash graphene. Nat Commun 15, 3218. https://doi.org/10.1038/s41467-024-47603-y.

[29] Silva, K.J., Wyss, K.M., Teng, C.H., Cheng, Y., Eddy, L.J., Tour, J.M., 2024. Graphene derived from municipal solid waste. Small, 2311021. https://doi.org/10.1002/smll.202311021.

[30] Eddy, L., Luong, D.X., Beckham, J.L., Wyss, K.M., Cooksey, T.J., Scotland, P., Choi, C.H., Chen, W., Advincula, P.A., Zhang, Z., Mancevski, V., Kittrell, C., Han, Y., Tour, J.M., 2024. Automated laboratory kilogram-scale graphene production from coal. Small Methods 8, 2301144. https://doi.org/10.1002/smtd.202301144.

[31] Zhan, B., Qu, Y., Qi, X., Ding, J., Shao, J., Gong, X., Yang, J.-L., Chen, Y., Peng, Q., Zhong, W., Lv, H., 2024. Mixed-dimensional assembly strategy to construct reduced graphene oxide/carbon foams heterostructures for microwave absorption, anti-corrosion and thermal insulation. Nano Micro Lett 16, 221. https://doi.org/10.1007/s40820-024-01447-9.

[32] Wu, Z., Tan, X., Wang, J., Xing, Y., Huang, P., Li, B., Liu, L., 2024. MXene hollow spheres supported by a C–Co exoskeleton grow MWCNTs for efficient microwave absorption, 107–107 Nano Micro Lett 16. https://doi.org/10.1007/s40820-024-01326-3.

[33] Wang, C., Han, X., Xu, P., Zhang, X., Du, Y., Hu, S., Wang, J., Wang, X., 2011. The electromagnetic property of chemically reduced graphene oxide and its application as microwave absorbing material. Appl Phys Lett 98, 072906. https://doi.org/10.1063/1.3555436.

[34] Huang, X., Yu, G., Zhang, Y., Zhang, M., Shao, G., 2021. Design of cellular structure of graphene aerogels for electromagnetic wave absorption. Chem Eng J 426, 131894. https://doi.org/10.1016/j.cej.2021.131894.

[35] Zhao, B., Li, Y., Zeng, Q., Wang, L., Ding, J., Zhang, R., Che, R., 2020. Galvanic replacement reaction involving core–shell magnetic chains and orientation-tunable microwave absorption properties. Small 16. https://doi.org/10.1002/smll.202003502.

[36] Zhang, F., Li, N., Shi, J.-F., Xu, L., Jia, L.-C., Wang, Y.-Y., Yan, D.-X., 2024. Recent progress on carbon-based microwave absorption materials for multifunctional applications: a review. Compos B Eng 283, 111646. https://doi.org/10.1016/j.compositesb.2024.111646.

[37] Tian, Y., Estevez, D., Wei, H., Peng, M., Zhou, L., Xu, P., Wu, C., Yan, M., Wang, H., Peng, H.-X., Qin, F., 2021. Chitosan-derived carbon aerogels with multiscale features for efficient microwave absorption. Chem Eng J 421, 129781. https://doi.org/10.1016/j.cej.2021.129781.

[38] Li, T., Zhi, D., Chen, Y., Li, B., Zhou, Z., Meng, F., 2020. Multiaxial electrospun generation of hollow graphene aerogel spheres for broadband high-performance microwave absorption. Nano Res 13, 477–484. https://doi.org/10.1007/s12274-020-2632-0.

[39] Gopakumar, D.A., Pai, A.R., Pottathara, Y.B., Pasquini, D., Carlos de Morais, L., Luke, M., Kalarikkal, N., Grohens, Y., Thomas, S., 2018. Cellulose nanofiber-based polyaniline flexible papers as sustainable microwave absorbers in the X-band. ACS Appl Mater Interfaces 10, 20032–20043. https://doi.org/10.1021/acsami.8b04549.

[40] Song, Q., Ye, F., Kong, L., Shen, Q., Han, L., Feng, L., Yu, G., Pan, Y., Li, H., 2020. Graphene and MXene nanomaterials: toward high-performance electromagnetic wave absorption in gigahertz band range. Adv Funct Mater 30, 2000475. https://doi.org/10.1002/adfm.202000475.

[41] Cao, M.-S., Cai, Y.-Z., He, P., Shu, J.-C., Cao, W.-Q., Yuan, J., 2019. 2D MXenes: electromagnetic property for microwave absorption and electromagnetic interference shielding. Chem Eng J 359, 1265–1302. https://doi.org/10.1016/j.cej.2018.11.051.

[42] Duan, W., Yin, X., Li, Q., Schlier, L., Greil, P., Travitzky, N., 2016. A review of absorption properties in silicon-based polymer derived ceramics. J Eur Ceram Soc 36, 3681–3689. https://doi.org/10.1016/j.jeurceramsoc.2016.02.002.

[43] Xu, L., Lin, Z., Chen, Y., Fan, Z., Pei, X., Yang, S., Kou, X., Wang, Y., Zou, Z., Xi, D., Yin, P., Su, G., Zhou, M., Dai, J., Pan, L., Zhao, Y., 2023. Carbon-based cages with hollow confined structures for efficient microwave absorption: state of the art and prospects. Carbon 201, 1090–1114. https://doi.org/10.1016/j.carbon.2022.10.015.

[44] Qin, M., Zhang, L., Wu, H., 2022. Dielectric loss mechanism in electromagnetic wave absorbing materials. Adv Sci 9. https://doi.org/10.1002/advs.202105553.

[45] Gao, Z., Ma, Z., Lan, D., Zhao, Z., Zhang, L., Wu, H., Hou, Y., 2022. Synergistic polarization loss of MoS2-based multiphase solid solution for electromagnetic wave absorption. Adv Funct Mater 32, 2112294. https://doi.org/10.1002/adfm.202112294.

[46] Zhao, T., Jia, Z., Liu, J., Zhang, Y., Wu, G., Yin, P., 2024. Multiphase interfacial regulation based on hierarchical porous molybdenum selenide to build anticorrosive and multiband tailorable absorbers, 6–6 Nano Micro Lett 16. https://doi.org/10.1007/s40820-023-01212-4.

[47] Feng, A., Lan, D., Liu, J., Wu, G., Jia, Z., 2024. Dual strategy of A-site ion substitution and self-assembled MoS2 wrapping to boost permittivity for reinforced microwave absorption performance. J Mater Sci Technol 180, 1–11. https://doi.org/10.1016/j.jmst.2023.08.060.

[48] Liang, L., Li, Q., Yan, X., Feng, Y., Wang, Y., Zhang, H.-B., Zhou, X., Liu, C., Shen, C., Xie, X., 2021. Multifunctional magnetic Ti3C2Tx MXene/graphene aerogel with superior electromagnetic wave absorption performance. ACS Nano 15 (4), 6622–6632 https://doiorg/10.1021/acsnano.0c09982.